

# Control of ion energy distributions using phase shifting in multi-frequency capacitively coupled plasmas

Yiting Zhang,<sup>1,a)</sup> Abdullah Zafar,<sup>2,b)</sup> David J. Coumou,<sup>3,c)</sup> Steven C. Shannon,<sup>2,d)</sup> and Mark J. Kushner<sup>1,e)</sup>

<sup>1</sup>Department of Electrical Engineering and Computer Science, University of Michigan, 1301 Beal Ave, Ann Arbor, Michigan 48109, USA

<sup>2</sup>Nuclear Engineering Department, North Carolina State University, 2500 Stinson Drive, Raleigh, North Carolina 27695, USA

<sup>3</sup>MKS Instruments, Inc. 100 Highpower Road, Rochester, New York 14623, USA

(Received 2 April 2015; accepted 5 June 2015; published online 17 June 2015)

Control of ion energy distributions (IEDs) onto the surface of wafers is an ongoing challenge in microelectronics fabrication. The use of capacitively coupled plasmas (CCPs) using multiple radio frequency (rf) power sources provides many opportunities to customize IEDs. In dual-frequency CCPs using a fundamental frequency and its second harmonic, varying the relative voltages, powers, and phases between the fundamental and second harmonic biases have demonstrated potential as control mechanisms for the shape of the IEDs. In this paper, we report on computational and experimental investigations of IED control in dual-frequency and triple-frequency CCPs where the phase between the fundamental and second harmonic frequency voltage waveform is used as a control variable. The operating conditions were 5–40 mTorr (0.67–5.33 Pa) in Ar and Ar/CF<sub>4</sub>/O<sub>2</sub> gas mixtures. By changing the phase between the applied rf frequency and its second harmonic, the Electrical Asymmetric Effects was significant and not only shifted the dc self-bias but also affected plasma uniformity. When changing phases of higher harmonics, the energies and widths of the IEDs could be controlled. With the addition of a 3rd high-frequency source, the plasma density increased and uniformity improved. Computed results for IEDs were compared with experimental results using an ion energy analyzer in systems using rf phase locked power supplies. © 2015 AIP Publishing LLC.

[<http://dx.doi.org/10.1063/1.4922631>]

## I. INTRODUCTION

Multi-frequency capacitively coupled plasmas (CCPs) are intended to provide independent control of the magnitude of ion and radical fluxes, and ion energy distributions (IEDs) incident onto wafers in microelectronics fabrication. Multi-frequency systems were motivated to overcome a weakness of single-frequency CCPs in which the magnitude of the ion fluxes and IEDs onto wafers are closely coupled.<sup>1,2</sup> In single-frequency systems, adjusting the bias power and frequency is the main method for controlling IEDs to match different process requirements.<sup>3,4</sup> Other methods of controlling IEDs with single frequency systems include the use of non-sinusoidal waveforms.<sup>5–7</sup> The typical dual-frequency CCP (DF-CCP) uses a low frequency (<a few MHz) to control the IEDs and a high frequency (>tens of MHz) to control the magnitude of the ion and radical fluxes.<sup>8</sup> However, even these choices of frequencies often result in the low frequency effecting the magnitude of ion fluxes and the high frequency affecting IEDs.<sup>9</sup>

With the goal of having finer control of IEDs, as characterized by the self-generated dc bias in CCPs, the electrical asymmetry effect (EAE) was developed by Heil *et al.*, a DF-CCP in which the frequencies consist of the fundamental frequency and its second harmonic.<sup>10</sup> Using this technique, the dc self-bias in geometrically symmetric, DF-CCPs can be controlled through control of the phase difference between the first and second harmonics. For example, the dc bias can be varied from positive-to-negative if the dual-frequencies are 13.56 and 27.12 MHz.<sup>10–13</sup> Heil *et al.* demonstrated that the EAE has the potential to separately control the magnitude of the ion flux and IEDs incident onto electrodes.<sup>10</sup> Several other studies have also investigated, both numerically and experimentally, the fundamentals and applications of the EAE.<sup>10–19</sup>

The EAE was initially investigated with a fundamental frequency of 13.56 MHz in geometrically symmetric CCPs to produce an asymmetric plasma response. Korolov *et al.* investigated the EAE by varying the fundamental frequency from 0.5 MHz to 60 MHz for CCPs sustained in argon at 375 mTorr (50 Pa) with an electrode gap of 2.5 cm.<sup>14</sup> Their simulations showed that a reduction in the ability to control the range of mean ion energies at lower fundamental frequencies resulted from the contributions of secondary electron emission. This reduced response at low frequencies was experimentally observed by Lafleur and Booth.<sup>15</sup> The EAE was

<sup>a)</sup>yitingz@umich.edu

<sup>b)</sup>azafar@ncsu.edu

<sup>c)</sup>David\_Coumou@mksinst.com

<sup>d)</sup>scshanno@ncsu.edu

<sup>e)</sup>Author to whom correspondence should be addressed. Electronic mail: mjckush@umich.edu

also investigated in a geometrically asymmetric chamber by Schüngel *et al.*<sup>16</sup> In experiments performed in Ar plasmas at 30 mTorr (4 Pa), they found that the EAE can still control the mean ion energies through adjusting the dc self-bias in asymmetric systems, though this control was limited by the natural negative dc-bias that is produced on the smaller electrode.

The EAE was also found to have utility for improving the uniformity of sputtering and thin film deposition. Bienholtz *et al.* investigated the EAE in a large area (500 mm diameter) multi-frequency CCP with an Ar/N<sub>2</sub> mixture at 22.5 mTorr (3 Pa), a chamber commonly used for sputter deposition processes.<sup>17</sup> Their system was operated with phase control between 13.56 MHz and 27.12 MHz. With Fourier analysis of the voltage waveforms for various phase angles, they found that not only the second harmonic, but also the amplitude and phase shift of higher harmonics had an influence on plasma density and dc self-bias. Although the electron density remained constant for a wide range of phase shifts, the plasma density increased by as much as 50% at specific phase shifts. Bienholtz *et al.* also reported on a challenge in controlling IEDs with the EAE due to the lack of control of currents produced at the higher harmonics. Hrunsk *et al.* reported favorable results for improved uniformity when applying the EAE to silicon thin film deposition in large area (1100 × 1400 mm) reactors.<sup>18,19</sup> The uniformity with 13.56 MHz + 27.12 MHz excitation was better than that produced by a single frequency 27.12 MHz discharge, an effect they attributed to a reduction in the standing wave effect found in high frequency, large area systems.

When controlling the phase between multiple frequencies, different varieties of non-sinusoidal waveforms can be generated for producing different plasma properties. Bruneau *et al.* reported producing an EAE-like effect when using up to 5 harmonics.<sup>20,21</sup> Their 1D particle-in-cell simulation predicted 50% higher ion flux on one electrode in geometrically symmetric CCPs when the sum of the harmonic frequencies had a specified phase shift. This effect was attributed to differing rising and falling slopes in time of the voltage waveform. At low pressure, longer mean free paths produced more uniform ionization and so more uniform sheath properties. When increasing the pressure in Ar plasmas from 20 to 800 mTorr (2.67 Pa to 106.66 Pa), ionization became more localized at both sheath edges and the asymmetry in ion flux became more pronounced. The asymmetry of the discharge decreased at lower fundamental frequencies as sheath heating no longer dominated the overall electron heating.

Prior investigations primarily focused on the influence of phase shifting on plasma properties with customized voltage waveforms over a large frequency range.<sup>22–25</sup> We follow those studies with an investigation of the consequences of the EAE on IEDs within the multiple rf frequencies of 15 + 30 MHz and 15 + 30 + 60 MHz. With plasma reactors in industry moving from DF-CCPs to triple frequency CCPs (TF-CCPs), the extension of the EAE to those systems would be beneficial. We report on experimentally measured plasma properties and IEDs, and results from computational investigations in both DF- and TF-CCPs with the phase shift with

respect to the harmonics ranging from 0° to 360°. We found that the dc self-bias varied with the modulation of the rf waveform as the EAE theory predicts in both DF- and TF-CCPs. The phase shifting of the harmonic frequencies also modulated the plasma densities and brought about a change in the sheath thickness. With the sheath thickness varying, the shape of the IEDs changed due to there being different ion transit times of ions of different masses through the sheath. The consequences of these trends on etch profiles is discussed.

In Sec. II, we summarize our computational methods, including both reactor scale model and profile simulators. The experimental setup and phase lock technology for phase control are described in Sec. III. Our results are discussed in Secs. IV (plasma properties in DF-CCPs) and V (plasma properties in TF-CCPs). Our concluding remarks are in Sec. VI.

## II. DESCRIPTION OF THE MODELS

For the reactor scale simulations described in this paper, we used the Hybrid Plasma Equipment Model (HPEM), a two-dimensional kinetic-fluid hydrodynamics code which combines separate modules that address different physical phenomena. HPEM has been previously described and so will be briefly summarized here.<sup>26</sup> For this study, the Electron Monte Carlo Simulation (eMCS), the Fluid Kinetics Poisson Module (FKPM) and the Plasma Chemistry Monte Carlo Module (PCMCM) were used to investigate EAE phenomena and ion energy distributions onto the substrate.

The FKPM solves separate continuity, momentum and energy equations for all heavy particle species (neutral and charged) while using drift-diffusion fluxes with the Sharffeter-Gummel formulation for electrons. Poisson's equation for the electric potential was solved using a semi-implicit technique with potentials evaluated at a future time with predicted densities of charged particles based on their current values and predictions based on time extrapolated fluxes. Since the highest frequency used in this study was 60 MHz and the chamber was only 150 mm in diameter, electromagnetic effects such as the standing wave effect were not included—our solution for electric potential is purely electrostatic. Time steps were chosen to be less than 1/300 of the highest applied frequency ( $1.1 \times 10^{-10}$  s for 30 MHz in DF-CCPs and  $5.5 \times 10^{-11}$  s for 60 MHz in TF-CCPs).

The electron energy distribution for both bulk and secondary electrons are derived completely kinetically in the eMCS including electron-electron collisions.<sup>27</sup> Particle trajectories for 4,000 to a maximum of 25,000 particles were integrated in time for more than 300 lowest frequency rf cycles on each call to the eMCS to produce spatially dependent electron energy distributions, which are then used to obtain electron impact source functions and transport coefficients. A separate Monte Carlo simulation was used for bulk electrons and for secondary, sheath accelerated electrons. These source functions and transport coefficients are then used in fluid equations for the bulk electron density. The boundary condition for our simulations is the voltage

waveform and so non-linearities in the system are reflected in the harmonic content of the current. For single frequency excitation for the experimental conditions, we compute significant current up to the 5th harmonic.

With a blocking capacitor connected in series to the bottom electrode in a geometrically asymmetric CCP, a dc self-bias was naturally generated on the electrode to balance currents collected by each electrodes. The dc bias ultimately determines the mean ion energy onto the substrate. The dc bias was determined by computing the time integral of the conduction and displacement current (net charge) collected by metal surfaces connected to either side of the capacitor

$$V_{dc} = \frac{1}{C} \int \sum_i m_i \left( \sum_j \vec{\phi}_j (q_j + q\gamma_{ij}) \cdot \hat{n}_i + \frac{\partial(\epsilon \vec{E} \cdot \hat{n}_i)}{\partial t} \right) dt, \quad (1)$$

where  $C$  is the blocking capacitance,  $\vec{\phi}_j$  is the flux of charged particle  $j$  having charge  $q_j$  incident onto metal  $i$  have local normal  $\hat{n}_i$ .  $\gamma_{ij}$  is the secondary electron emission coefficient for species  $j$  and metal  $i$ . The first summation is over metal surfaces, where  $m_i$  is  $\pm 1$  depending on whether the metal is on the grounded or powered side of the circuit. The second summation is over charged species.

When investigating the consequences of phase shift between the fundamental and second harmonic frequencies, the voltage waveform on the bottom electrode is expressed as

$$V_B(t) = V_{LF} \sin(\omega_{LF}t + \phi_{LF}) + V_{HF} \sin(\omega_{HF}t + \phi_{HF} + \Delta\phi_{HF}), \quad (2)$$

where  $LF$  refers to the low frequency and  $HF$  refers to the high frequency.  $\phi_{LF}$  and  $\phi_{HF}$  refer to the unknown phase offset from the signal generator to the electrode through the transmission line in the experiment for each frequency. Having no other information, these phase offsets are assumed to be the same.  $\Delta\phi_{HF}$  refers to the shift in the phase of the  $HF$  with respect to the  $LF$ . Unless noted otherwise, in the computations  $LF = 15$  MHz and  $HF = 30$  MHz.

In the TF-CCP, a sinusoidal 60 MHz waveform was applied on the top electrode, which is expressed as

$$V_T(t) = V_{60} \sin(\omega_{60}t + \phi_{60} + \Delta\phi_{60}), \quad (3)$$

where  $\phi_{60}$  refers to the phase offset from the 60 MHz signal generator and  $\Delta\phi_{60}$  refers to the shift in the phase of the 60 MHz with respect to the 15 MHz voltage. In the experiment, phase locks were only used on the fundamental and second harmonic frequencies. Therefore, the phase offset and phase shift of 60 MHz are unknown. The influence of the 60 MHz phase shift was investigated with the model and will be discussed in Sec. IV.

The PCMCM was used to obtain the ion and neutral fluxes as well as their energy and angular distributions onto surfaces in contact with the plasma. All simulated IEDs presented in this paper are normalized to their maximum value and averaged over the surface of the substrate.

The majority of the simulations were performed in pure argon with species consisting of Ar, Ar(1s<sub>2</sub>), Ar(1s<sub>3</sub>), Ar(1s<sub>4</sub>), Ar(1s<sub>5</sub>), Ar(4p,5d), Ar<sup>+</sup> and e. The reaction mechanism for Ar is essentially the same as described in Ref. 28. In addition to the pure argon cases, an Ar/CF<sub>4</sub>/O<sub>2</sub> gas mixture was also simulated to study the influence of the EAE on plasma etching process. The gas phase and surface reaction mechanisms are discussed in Refs. 27 and 29. The species in the Ar/CF<sub>4</sub>/O<sub>2</sub> mechanism were Ar, Ar(1s<sub>5</sub>, 1s<sub>3</sub>) metastable, Ar(1s<sub>2</sub>, 1s<sub>4</sub>) radiative, Ar(4p,5d), Ar<sup>+</sup>, CF<sub>4</sub>, CF<sub>3</sub>, CF<sub>2</sub>, CF, C, F, F<sub>2</sub>, C<sub>2</sub>F<sub>4</sub>, C<sub>2</sub>F<sub>6</sub>, C<sub>2</sub>F<sub>8</sub>, SiF<sub>4</sub>, SiF<sub>3</sub>, SiF<sub>2</sub>, CF<sub>3</sub><sup>+</sup>, CF<sub>2</sub><sup>+</sup>, CF<sup>+</sup>, C<sup>+</sup>, F<sup>+</sup>, F<sub>2</sub><sup>+</sup>, CF<sub>3</sub><sup>-</sup>, F<sup>-</sup>, O<sub>2</sub>, O<sub>2</sub>(<sup>1</sup>Δ), O<sub>2</sub><sup>+</sup>, O, O(<sup>1</sup>D), O<sup>+</sup>, O<sup>-</sup>, COF, COF<sub>2</sub>, CO<sub>2</sub>, FO and e.

Energy and angular distributions incident onto the substrate for Ar<sup>+</sup>, CF<sub>3</sub><sup>+</sup>, CF<sub>2</sub><sup>+</sup>, CF<sup>+</sup>, F<sup>+</sup> and F<sub>2</sub><sup>+</sup> and major neutral particles produced by the PCMCM were transferred to the Monte Carlo Feature Profile Model (MCFPM). MCFPM is a 2 dimensional profile simulator which is used to predict profile evolution during etching, in this case etching SiO<sub>2</sub> over Si.<sup>30</sup> In the MCFPM, the surface materials of the wafer are resolved with a rectilinear mesh. Each mesh cell represents a different solid material. Pseudo-particles were launched towards the surface with velocities randomly selected from the energy and angular distributions provided by the PCMCM. The particle identity was randomly chosen from the mole-fraction weighted fluxes of all incident species. When the pseudo-particle strikes a solid cell, the particle may reflect, chemically react, adsorb, sputter or implant based on the randomly allocated probabilities of the reaction mechanism. The reaction mechanism for etching of Si and SiO<sub>2</sub> in fluorocarbon plasma is described in detail in Ref. 31. In order to eliminate the effect of mask erosion on etch profiles, we assumed a hard mask that does not change its shape during processing.

### III. DESCRIPTION OF THE EXPERIMENT

Measurements of IEDs incident onto the substrate and dc biases were made in a parallel plate CCP. The apparatus could be powered by 3-separate voltage sources, typically a fundamental and its second harmonic, and a  $HF$ . Control algorithms were developed to enable phase locking of the fundamental and the second harmonic. The DF-CCP has been previously reported and described in detail in Ref. 32. The TF experimental setup is shown in Fig. 1 and comprises the following subsystems: (1) plasma source with vacuum regulation and gas flow control; (2) very high frequency (VHF) power supply and impedance matching network; (3) phase-locked, harmonic drive rf power supply and associated dual frequency matching network; and (4) metrology comprising an energy analyzer and rf sensors.

#### A. Capacitively coupled plasma source

All experiments were performed on the Modular Radiofrequency Plasma Chamber (MrPC). MrPC is a parallel plate CCP reactor with two 150 mm diameter aluminum electrodes. The electrodes are mechanically fastened to spindles for adjusting the distance between the electrodes and their position inside the reactor. The electrode gap was

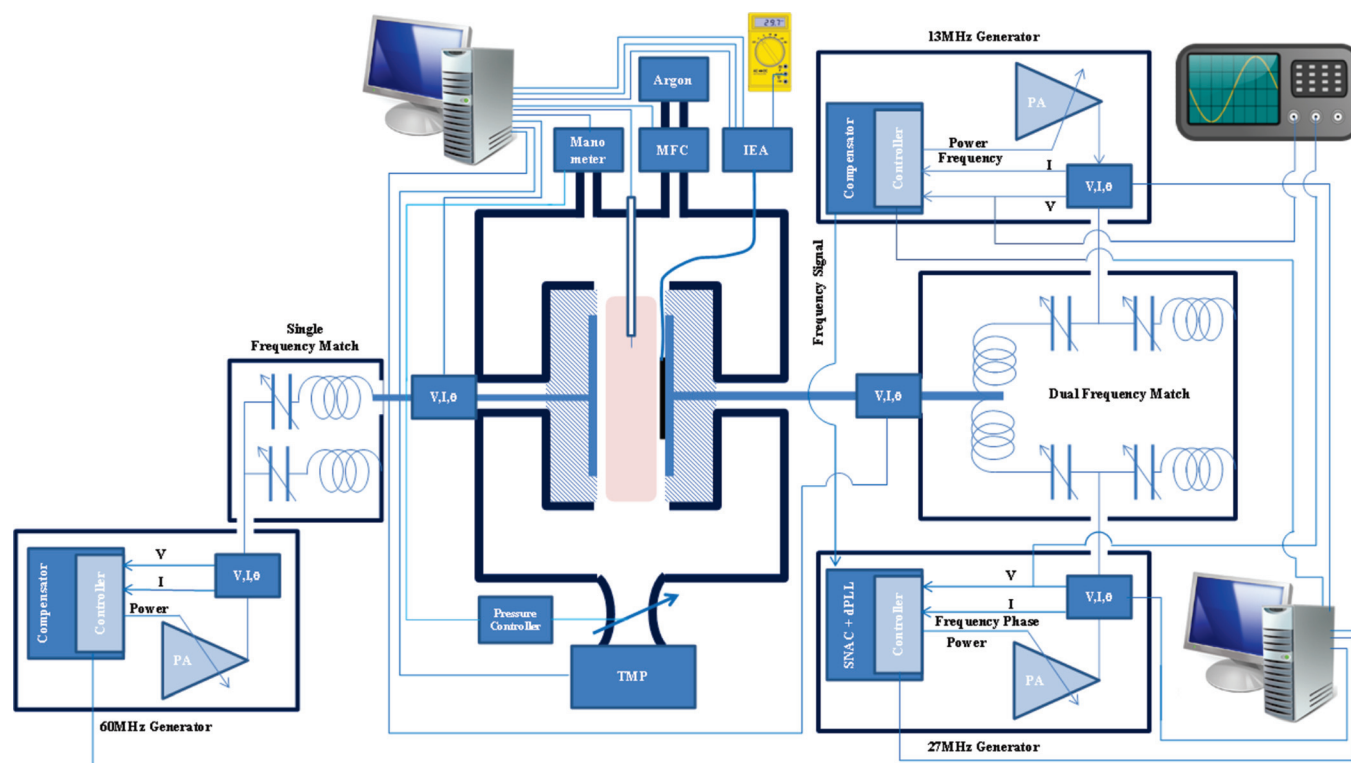


FIG. 1. Experimental setup for triple frequency CCP. Dual frequency setup is similar except that the top electrode is grounded.

2.54 cm for the DF investigation and 1.9 cm for the TF investigation. The electrodes are housed in a Rexolite plastic shroud that provides 180 pF of electrical isolation to the surrounding ground plate with an approximate loss tangent of 0.001 at 100 MHz. The powered electrodes are coupled to their respective matching networks through RG-393 MIL-C-17 rf cable and terminated on each end with N-Type connectors. The reactor can sustain a plasma source from excitation frequencies ranging from 100 kHz to 200 MHz. MrPC is a stainless steel vessel pumped by a turbo molecular pump (TMP) with a base pressure of  $<0.1$  mTorr. The leak rate of the reactor when isolated from the TMP was 1.4 mTorr/min. The associated gas introduced into the system by this small leak is negligible compared to the controlled gas flow for all experiments. All experiments were conducted with argon, supplied to the chamber using an analog controlled mass flow controller. Pressure was controlled using a closed-loop capacitance manometer and throttle valve for pressure measurement and conductance control, respectively. For this experiment, this feedback system was used to maintain reactor pressure at a given set-point.

In the TF configuration, the electrode on the left side of the reactor, schematically shown in Fig. 1, is coupled to the 60 MHz rf power supply for plasma generation. This AE Ovation 5060 60 MHz power supply transfers rf power to the electrode through an auto-tuning matching network. The counter electrode is coupled to the phase-locked harmonic driven rf power delivery system, which consists of frequency agile 13.56 MHz Surepower and 27.12 MHz LVG rf generators from MKS Instruments, Inc., ENI Products. The harmonic rf power delivery is coupled to the electrode through

a DF matching network. A computer interface is networked to the rf power supplies to configure power and phase settings.

## B. Phase locked, harmonic drive rf power delivery

The frequency and phase locking technology is based on a digital phase-locked loop<sup>32</sup> (dPLL). The harmonic rf power delivery system is composed of two frequency agile rf supplies. The 13.56 MHz rf generator is designated as the master and the 27.12 MHz rf power supply is the slave. This rf excitation signal is sampled by the slave generator, converting it to a digital signal and processing it along with a digital representation of the local rf it generates. To create a harmonic replica of the master frequency, the slave controller applies a digital phase-locked loop to synchronize and scale the local frequency to the excitation signal. Before employing the phase-locked loop, digital signal processing is applied for immunity from spurious frequency content arising from the frequencies supplied by the generators and the corresponding harmonic and mixing frequency emission from the sheath dynamics.<sup>33</sup> In the slave controller, digital down-conversion is separately performed for the sampled excitation signal and the local frequency generated by the slave. This digital process down-sampled the digital signals from the A/D conversion rate to an integer divisible sample rate. While lowering the data rate, a variable narrowband filter attenuates the spurious frequencies to retain a digital baseband signal. This digital process is followed for both the excitation signal and the local rf signal. The digital baseband signals are represented in a mathematically complex form and applied to the digital phase-locked loop. To determine the frequencies of each

signal, the time derivative of the phasor of each digital base-band signal was computed. This provides a measure of the excitation signal frequency,  $f_e = \frac{\partial \theta_e(t)}{2\pi \partial t}$ , and the local slave frequency,  $f_{rf} = \frac{\partial \theta_{rf}(t)}{2\pi \partial t}$ . To adjust the local frequency of the slave output power to the excitation signal, a frequency error,  $f_\Delta = f_e - f_{rf}$ , was computed and applied to a proportional, integral, and derivative (PID) controller<sup>34</sup> that iteratively produces updates to a digital synthesizer generating the frequency of the slave power supply. As the frequency converges to the harmonic of the master frequency, the frequency error  $f_\Delta \rightarrow 0$ .

Once the slave frequency is locked, the dPLL transitions to phase control. The output phase of the rf is compared to the desired phase and maintains this set point through transient conditions and systematic effects. One systematic influence is attributed to the power amplifier (PA). In PA circuits, there is a phase shift related to the amount of output power. In conventional rf plasma discharges, this phase shift is irrelevant. To tailor the skew of the IEDs based on phase shift between the harmonic pair; this systematic offset can impair the target distribution. The relationship between the master and slave generators is a normalization of this phase shift of the PA circuit only (no active phase control) as it relates to the normalized power generated. The phase shift rapidly decreases at lower power before the monotonic effect reduces for mid- to higher-power range. The phase shift is due to the output capacitance of MOSFET devices used in PA circuits.<sup>35</sup> Our dPLL generates the harmonic frequency and accurately maintains the target phase output relationship with the coupled excitation signal from the slave. The benefit is substantial enough to gain a higher degree of fidelity in generating the desired IED.

### C. Metrology

The metrology for our experiments served two objectives: (1) monitor and control the rf power and (2) measure plasma parameters, specifically, the ion energies we sought to manipulate for IED control. To monitor the rf source power for each electrode, in-line rf metrology was connected at the output of each impedance matching network as shown in Fig. 1. To facilitate rf measurements in the range of 13.56 MHz to 60 MHz, rf metrology comprised broadband VI sensors and accompanying signal processing from MKS Instruments, Inc. To alleviate out-of-band spectrum from impinging measurements at the frequency of interest, narrow-band digital filters were configured in a parallel digital signal processing architecture for high-data rate results with high accuracy.<sup>36</sup> An rf-compensated Langmuir probe, positioned at the center of the discharge, was used to measure electron density, electron temperature, and plasma potential. IEDs were measured with a Retarding Field Energy Analyzer (RFEA), which was positioned on the biased electrode. The ion energy measurement system was from Impedans Ltd. and the sensor was constructed with an array of holes for ion absorption at the plasma interfacing surface, above the multi-layer ion collector within the sensor cavity.<sup>37</sup>

## IV. PLASMA PROPERTIES AND IEDS IN A DF-CCP REACTOR

Schematics of the two-dimensional, cylindrically symmetric DF- and TF-CCPs used in the simulation are shown in Fig. 2. In the DF-CCP, the gap between the electrodes was 2.54 cm to match the experiments. Gas was injected through the top nozzle at 50 sccm near the chamber wall. The top electrode and the metal wall were grounded, and thus the CCP reactor is geometrically highly asymmetric. Both rf biases were applied to the bottom electrode through a blocking capacitor (1  $\mu$ F). The 15 cm in diameter substrate was surrounded by a dielectric focus ring ( $\epsilon/\epsilon_0 = 2.53$ ,  $\sigma = 10^{-9} \Omega^{-1} \text{cm}^{-1}$ ). The annular pump port was at the bottom of the computational domain, coaxially surrounding the substrate. During execution of the code, the flow rate through the pump port, also nominally 50 sccm, was adjusted to keep the pressure inside the plasma chamber constant.

Operating conditions for the TF-CCP were nearly same as for the DF-CCP, except that the gap was 1.90 cm and a 60 MHz rf source was applied to the top electrode. All results from the experiment were obtained with 13.56 MHz + 27.12 MHz power applied to the bottom electrode and an optional 60 MHz on the top electrode for TF-CCP. For reasons having to do with computational alignment of frequencies and minimizing numerical error, the lower two rf frequencies in the simulation were rounded to 15 MHz and 30 MHz. The phase shift between the harmonics was at 30° increments for both the simulation and experiments.

The experimental chamber is highly asymmetric. That is, the area ratio between the grounded surfaces and power electrode(s) greatly exceeds unity, and this naturally produces a dc bias. The entire volume of the reactor exceeds what can be realistically included in the numerical mesh of

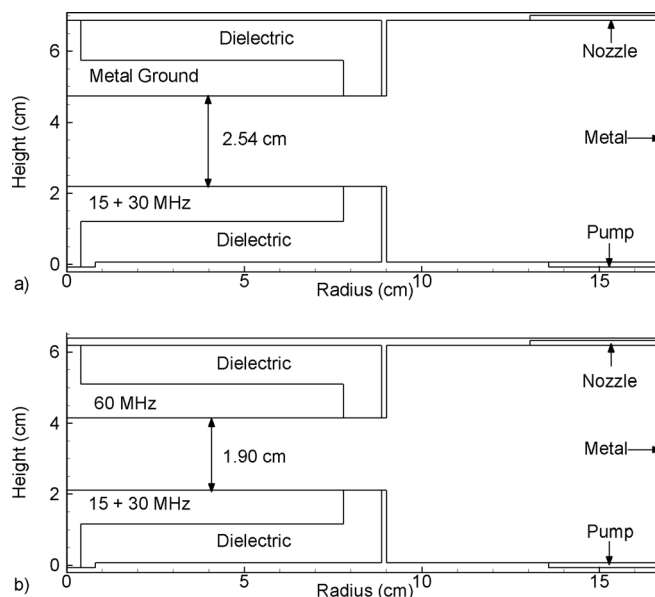


FIG. 2. Schematic of geometries used in the model. (a) Dual frequency CCP with both 15 and 30 MHz applied on the bottom electrode. The top electrode and metal chamber wall are grounded. The gap between the two electrodes is 2.54 cm. (b) Triple frequency CCP with 15 and 30 MHz applied on the bottom electrode, and 60 MHz applied on the top electrode. The electrode gap is 1.9 cm. The chamber wall is grounded.

our model. The result is that the area of grounded surfaces in the model is smaller than in the experiment. Therefore, for a given applied voltage, we will not produce the same dc-bias as in the experiment. The primary objective of this study is the behavior of the IEDs which are most sensitive to the dc bias. We therefore chose voltages in the model to match the base case dc bias in the experiment. This difference in voltage amplitude has an effect on predicted plasma densities, as discussed below.

To validate the HPEM and, in particular, the PCMCM that produces IEDs, a set of single frequency simulations were performed with pressures ranging from 10 to 40 mTorr (1.33 Pa to 5.33 Pa) of Ar with a flow rate of 50 sccm. The power was 100 W at 30 MHz. The dc self-bias was kept at a constant value of  $-87$  V in the simulation. The simulated IEDs, shown in Fig. 3(a), agree favorably with previously published experimental results.<sup>32</sup> To better visually match the presentation of the experimental results, the simulated IEDs were normalized to 1.0 at their maximum values. For these single frequency IEDs, the bimodal distribution typically obtained at low frequencies has already started merging towards a single peak. For a dc bias of  $-87$  V and the time averaged plasma potential of 35 V, the average ion energy

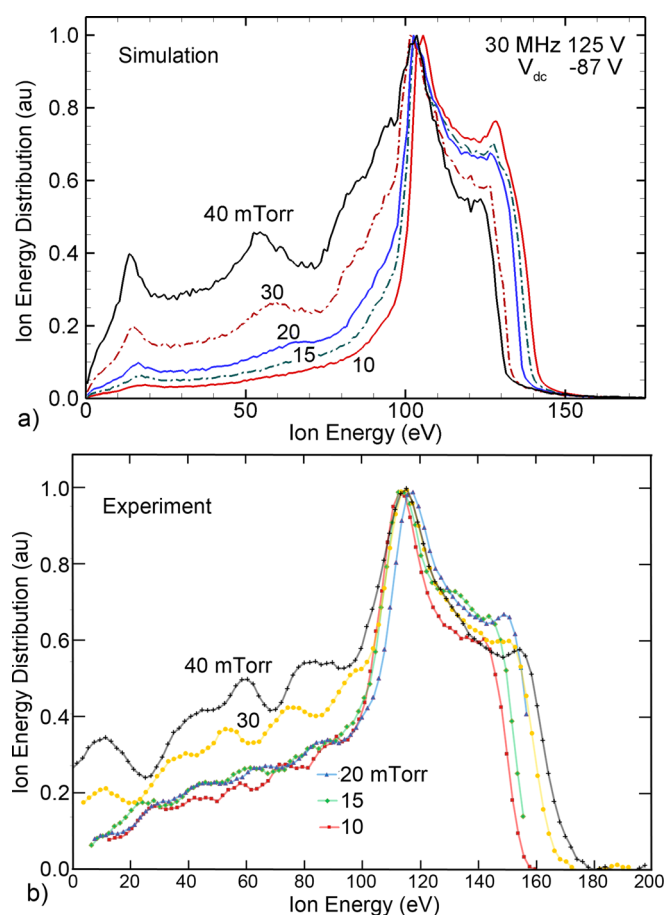


FIG. 3. IEDs for a single frequency CCP with pressure varying from 10 to 40 mTorr. Power was varied to provide constant dc bias voltage ( $-87$  V) for each condition. (a) Simulated IEDs for an Ar plasma with 30 MHz on the bottom electrode. (b) Experimental results. Reprinted with permission from D. J. Coumou *et al.*, IEEE Trans. Plasma Sci. **42**, 1880 (2014). Copyright 2014 IEEE.

should be near 122 V, which is about the location of the peak of the IED. With constant power at high pressure, ion-neutral collisions produce modulation in the IEDs at energies of  $<70$ – $80$  eV.<sup>38</sup> With a decrease in pressure, the ion mean free path increases and exceeds the sheath thickness. The sheath on the powered substrate transitions from collisional to less-collisional, and the low energy tail of IEDs is less modulated when the pressure is below 20 mTorr. Because the RFEA system requires a balance between minimizing collisional distortion and maximizing ion fluxes, all DF/TF phase-locked simulations and experiments were conducted between 10 and 20 mTorr.

The mismatch in the maximum energy between the simulation and experiment results from some inherent differences in the mode of operation in the experiment and in the simulations. In the experiments, current is the independent variable and power the dependent variable. In the simulations, power is the independent variable and current is the dependent variable. (Changing the mode of operation of the model to current being the independent variable was beyond the scope of this study.) As such, it is sometimes difficult to exactly match the operating conditions of the experiment with the simulations.

To provide a perspective for our investigation of EAE characteristics, a base case simulation was performed for Ar at 20 mTorr and 50 sccm flow. The waveform for the DF excitation was  $V_B(t) = 100V \sin(\omega_{15}t + \phi_{15}) + 100V \sin(\omega_{30}t + \phi_{30} + \Delta\phi_{30})$ , where the phase offset of the signal generator to the electrode,  $\phi_{15} = \phi_{30} = 180^\circ$  and there is no phase shift  $\Delta\phi_{30}$  between the 15 and 30 MHz signals. ( $V_B(t)$  is the voltage on the bottom electrode.) The electron density,  $n_e$ , electron temperature,  $T_e$ , ionization by bulk electrons,  $S_e$ , and ionization by secondary electrons (secondary emission coefficient  $\gamma = 0.15$ ),  $S_{sec}$ , for this base case are shown in Fig. 4. With an equal voltage for each of the dual-frequencies, the plasma density was approximately  $10^{11} \text{ cm}^{-3}$  with an average bulk electron temperature of  $T_e = 3.3 \text{ eV}$ . The bulk ionization source, maximum of  $1 \times 10^{16} \text{ cm}^{-3} \text{ s}^{-1}$  is about two orders larger than the ionization by secondary electrons.

The electron density predicted by the model is larger than that measured using probes for similar conditions, which is  $2 \times 10^{10} \text{ cm}^{-3}$ . The experimental voltage amplitudes for each frequency is about 40 V for those measurements. When using a 40 V amplitude in the model, the predicted electron density drops to  $5 \times 10^{10} \text{ cm}^{-3}$ , which is within about a factor of 2 of the measurement. As mentioned above, the main object of this study is understanding the IEDs which are most sensitive to the value of the dc bias. Due to the differences in the area of the grounded surfaces of the reactor between the model and the experiment (see prior discussion), we adjusted the voltage in the model for the base case to 100 V in order to produce an initial dc self-bias similar to that of the experiment. This increase in voltage accounts for about a factor of two increase in plasma density above that of the experiment.

With  $\Delta\phi_{30}$  varied from  $0^\circ$  to  $360^\circ$  with  $\phi_{15} = \phi_{30} = 180^\circ$ , the dc self-bias is shown in Fig. 5(a). The results from the simulation and the experiment agree well. Due to

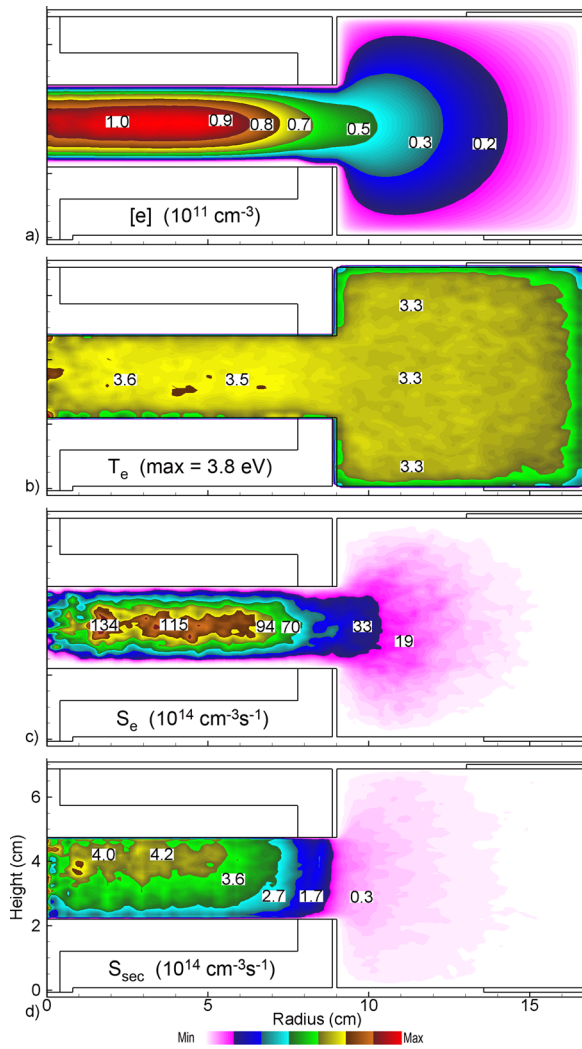


FIG. 4. Time averaged plasma properties for the DF-CCP having base case conditions (Ar, 20 mTorr, 50 sccm,  $V_{bottom}(t) = 100V \sin(\omega_{15}t + 180^\circ) + 100V \sin(\omega_{30}t + 180^\circ)$ , no phase shift between two frequencies). (a) Electron density, (b) electron temperature, (c) bulk electron ionization source, and (d) ionization by sheath accelerated secondary electrons. The plots use linear scales.

the reactor being highly asymmetric, a dc self-bias is naturally generated to balance currents on both electrodes even with no phase shift. The consequences of the EAE adds to or subtracts from the zero-phase dc bias, which in this case is negative. Therefore, the dc-self bias is always negative in the simulations and measurements. As the EAE theory predicts, the dc self-bias linearly depends on the phase angle of the 15 MHz. However, we observed that the dc self-bias shows a sinusoidal-like variation with the phase angle of 30 MHz varying from  $0^\circ$  to  $360^\circ$ . We also performed simulations with a phase offset  $\varphi_{15} = \varphi_{30} = 0^\circ$  and  $90^\circ$  (i.e., waveforms that are sine and cosine functions with different amplitudes) as shown in Fig. 5(b). Although dc self-biases show linear modulation at certain phases, most simulated dc-self biases show sinusoidal-like variations, which can be expressed as a sine function with its phase offset equal to the rf phase offset  $\varphi$ .

The amplitude of the variation in dc self-bias depends on the voltage amplitude of the 15 MHz and 30 MHz biases. When both voltage amplitudes are increased to 150 V, the

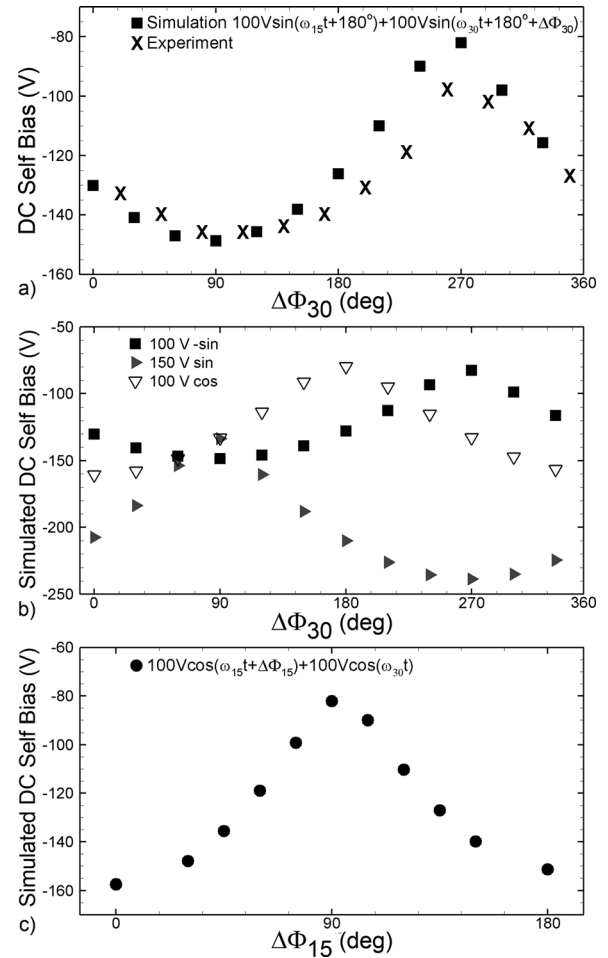


FIG. 5. Dc self-biases with a shift of phase  $\Delta\Phi_{30}$  from  $0^\circ$  to  $360^\circ$ . (a) Simulated and measured dc self-biases for base case operating conditions. (b) Simulated dc self-biases for different sinusoidal waveforms (different phase offset). The “100 V-sin” represents  $V_B(t) = 100V \sin(\omega_{15}t + 180^\circ) + 100V \sin(\omega_{30}t + 180^\circ + \Delta\Phi_{30})$ , the “150 V sin” represents  $V_B(t) = 150V \sin(\omega_{15}t) + 150V \sin(\omega_{30}t + \Delta\Phi_{30})$ , and “100 V cos” represents  $V_B(t) = 100V \cos(\omega_{15}t) + 100V \cos(\omega_{30}t + \Delta\Phi_{30})$ . (c) Simulated dc self-biases for cosine functions with phase shift angle applied at the fundamental frequency:  $V_B(t) = 100V \cos(\omega_{15}t + \Delta\Phi_{15}) + 100V \cos(\omega_{30}t)$ .

rf currents on the electrode are increased for all phase shifts. Thus, more negative dc self-biases are produced for all phase shifts for bias waveforms  $V_B(t) = 150V \sin(\omega_{15}t) + 150V \sin(\omega_{30}t + \Delta\Phi_{30})$ . With the application of cosine functions (i.e.,  $V_B(t) = 100V \sin(\omega_{15}t + 90^\circ) + 100V \sin(\omega_{30}t + 90^\circ + \Delta\Phi_{30})$ ), the simulated dc self-bias modulation is close to the measured and simulated results of Schulze *et al.*<sup>39</sup> Ultimately, the dc bias at zero-phase (or a reference phase) is determined by the area ratios of the powered and grounded surfaces. The change in dc bias as a function of  $\Delta\phi$  from the reference value then depends on the shape of the voltage wave form (e.g., sine vs cosine) and which phase is being varied (fundamental or second harmonic). The simulated results show that the dc self-bias varies linearly for most phase angles and shows sinusoidal-like shapes at other phase angles. These results suggest the linear dependence between dc self-bias and phase does not strictly hold as the waveform and geometrical conditions (e.g., symmetric vs asymmetric) change.

For example, in many prior studies of EAE, the basic voltage waveforms have zero phase offset at the fundamental and second harmonic, and the phase variation is applied to the fundamental. With all other conditions kept the same, we used this form of the bias waveform in the model:  $V_B(t) = 100V \cos(\omega_{15}t + \Delta\phi_{15}) + 100V \cos(\omega_{30}t)$ . The predicted variation in dc self-biases, shown in Fig. 5(c), agree well with the theoretical prediction. When  $\Delta\phi_{15}$  is shifted from  $0^\circ$  to  $90^\circ$ , the dc self-bias becomes 75 V less negative, which shows a similar trend to the 1-D simulations of an asymmetric CCP.<sup>40</sup>

This part of study suggests that the value of dc-self bias is determined by two kinds of asymmetries, electrical and geometrical. By adjusting phases, the electrical asymmetry effect modulates dc self-bias. Many previous studies have investigated EAE in geometrically symmetric reactors which do not have an initial dc self-bias resulting from the geometrical asymmetry. With the initial dc self-bias equal to zero, the EAE can tailor the dc self-bias to be either positive or negative. On the other hand, the initial value of dc self-bias is determined by the amplitude of the rf current and the geometrical asymmetry. In this case, the EAE modulates the dc bias but does not necessarily provide a full dynamic range from negative to positive.

The unknown phase offset in the experiment can be estimated by the variation in the dc bias starting phase at  $\Delta\phi_{30} = 0^\circ$  if the phase offsets of both frequencies are the same. Since current is controlled in the experiment, the amplitudes of both frequencies had about a 15% variation during the parameterization of  $\Delta\phi_{30}$ . This variation may explain why at certain values of  $\Delta\phi_{30}$  there is less good agreement between the model and experiment. Other differences include the geometry of the reactor which in part determines the dc bias ( $|V_{dc}| \propto \frac{A_{ground}}{A_{power}}$ ). Due to computational limitations, the surface area of the grounded chamber walls is smaller in the model than in the experiment.

For otherwise the same conditions, the computed plasma density and uniformity were affected by phase shifting, as shown in Fig. 6. The electron densities were recorded as a function of radius to the edge of the substrate in the middle of the electrode gap. The plasma densities remained constant for the majority of the values of  $\Delta\phi_{30}$  between  $0^\circ$  and  $180^\circ$ , with a maximum value of  $1.1 \times 10^{11} \text{ cm}^{-3}$  at a radius of about 5 cm. At larger phase differences, the plasma density increased by 40% to  $1.35 \times 10^{11} \text{ cm}^{-3}$  with the maximum shifting to the center of the reactor. A similar phenomenon was measured and reported by Bienholz *et al.*<sup>17</sup> Keeping the voltage constant while providing different rf voltage waveforms with different  $\Delta\phi_{30}$  produces different power deposition and different spatial distributions of ionization that provide larger instantaneous ionization rates. The cycle averaged ionization rates for bulk electrons for  $\Delta\phi_{30} = 90^\circ$  and  $270^\circ$  are shown in Fig. 6. (Recall that the plasma density is mainly produced by bulk ionization.) The ionization rates for  $\Delta\phi_{30} = 90^\circ$  have a maximum near 5 cm that corresponds to the maximum in electron density. In contrast, the time averaged bulk ionization source for  $\Delta\phi_{30} = 270^\circ$  has a maximum near the axis, which corresponds to the peak in electron density for that phase offset. These results align with changes in

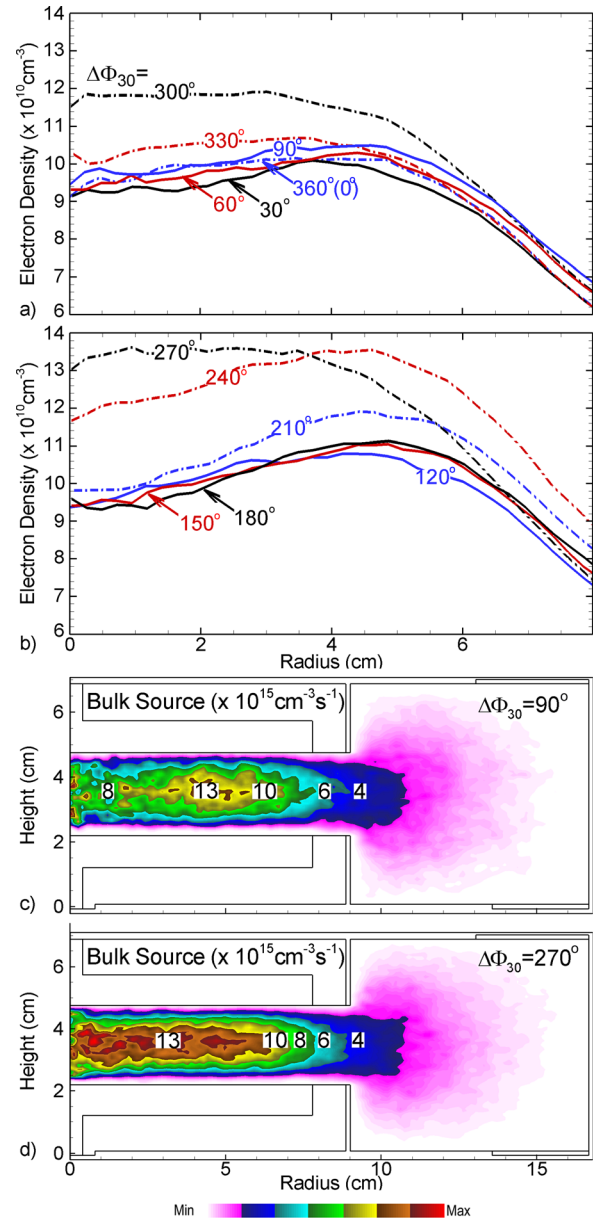


FIG. 6. Time averaged electron density in the middle of the electrodes (1.27 cm above substrate) from the center to the edge of the substrate for Ar, 20 mTorr, 50 sccm with rf bias:  $V_B(t) = 100V \sin(\omega_{15}t + 180^\circ) + 100V \sin(\omega_{30}t + 180^\circ + \Delta\phi_{30})$ . (a)  $\Delta\phi_{30} = 300^\circ, 330^\circ, 360^\circ(0^\circ), 30^\circ, 60^\circ, 90^\circ$ . (b)  $\Delta\phi_{30} = 120^\circ, 150^\circ, 180^\circ, 210^\circ, 240^\circ$ , and  $270^\circ$ . Note that the range of density plotted is from  $6 \times 10^{10}$  to  $14 \times 10^{10} \text{ cm}^{-3}$ . (c) Cycle averaged bulk ionization source for  $\Delta\phi_{30} = 90^\circ$  and (d)  $\Delta\phi_{30} = 270^\circ$ .

the spatial dependence of the electron energy distribution with phase offset.

We also investigated the sheath dynamics for different  $\Delta\phi_{30}$ . The rf waveforms for  $\Delta\phi_{30} = 90^\circ$  and  $270^\circ$  are shown in Fig. 7(a). The electron densities in the near sheath region (0–4 mm above the substrate) at the bullet-marked times are shown in Fig. 7(b). The  $\Delta\phi_{30} = 90^\circ$  voltage waveform spends the majority of the cycle below zero. This produces a longer cathodic portion of the cycle and more sheath expansion from  $t = 0$  to  $0.63T_{15}$  ( $T_{15}$  is one 15 MHz period). At  $t = 0.63T_{15}$ , electrons start to re-enter the sheath and the sheath collapses at  $t = 0.75T_{15}$  when the most positive bias is applied. After that time, the sheath starts to expand again

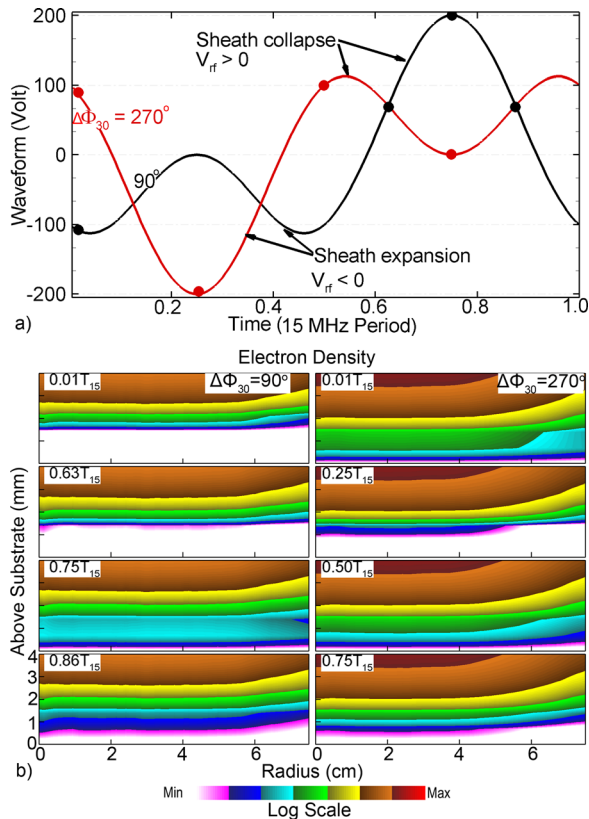


FIG. 7. Sheath dynamics for  $\Delta\phi_{30} = 90^\circ$  and  $270^\circ$  during one 15 MHz period,  $T_{15}$ . (a) rf waveform applied to the substrate. (b) Electron density in the sheath region (radius from 0 to 7.5 cm and height from 0 to 4 mm above the substrate) for selected time points for (left)  $\Delta\phi_{30} = 90^\circ$  and (right)  $\Delta\phi_{30} = 270^\circ$ .

and the sheath boundary moves back towards the bulk plasma. Unlike the  $\Delta\phi_{30} = 90^\circ$  voltage waveform, the cathodic portion of the cycle is shorter for  $\Delta\phi_{30} = 270^\circ$ . As a result, the sheath is collapsed for the majority of the 15 MHz period. The sheath for  $\Delta\phi_{30} = 90^\circ$  is generally thicker than for  $\Delta\phi_{30} = 270^\circ$  due to a lower plasma density and much longer cathodic phase. Since the ion transit time through the sheath depends on the sheath thickness and when ions enter the sheath, these sheath dynamics produce significant variations of the IEDs.

The computed IEDs corresponding to variation in  $\Delta\phi_{30}$  are shown in Fig. 8. Three phenomena occur when  $\Delta\phi_{30}$  is varied that can affect the IEDs. First, the variation in dc self-bias produces a change in the modulation of the sheath potential and therefore, the mean ion energy. For example, the high energy tail of the IEDs shifts by about 70 eV which tracks the change in the dc self-bias with change in  $\Delta\phi_{30}$ . The increase in dc bias for  $\Delta\phi_{30} = 90^\circ$  to  $-150$  V correlates with the extension of the IED to 220 eV. Second, the IEDs are 10 to 20 eV wider in energy at phases  $\Delta\phi_{30} = 0^\circ - 120^\circ$ . The energy width  $\Delta E \propto \sqrt{n_e \bar{V}_s}$ . The plasma densities at those phases are lower and so their sheaths are thicker, which can contribute to narrower energy widths. However, the average sheath voltages are higher at those phases. This is the main determining parameter for our operating conditions. Thus, the energy width slightly modulates at certain phases. Third, the shape of IEDs is not consistent across phase

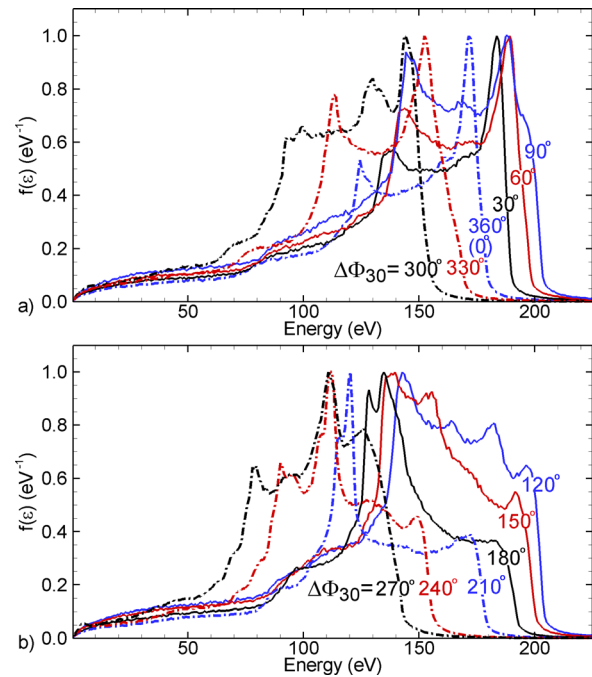


FIG. 8. Time averaged IEDs onto the substrate for Ar at 20 mTorr, 50 sccm with rf bias:  $V_B(t) = 100V \sin(\omega_{15}t + 180^\circ) + 100V \sin(\omega_{30}t + 180^\circ + \Delta\phi_{30})$ . (a)  $\Delta\phi_{30} = 300^\circ, 330^\circ, 360^\circ (0^\circ), 30^\circ, 60^\circ, 90^\circ$ . (b)  $\Delta\phi_{30} = 120^\circ, 150^\circ, 180^\circ, 210^\circ, 240^\circ, 270^\circ$ .

changes. The energy at which the IED is maximum shifts with  $\Delta\phi_{30}$ . This shift is mainly due to the high frequency modulation of the sheath potential by the 30 MHz voltage.

Selected results from the experiment for IEDs are compared with results from the simulation in Figs. 9(a) and 9(b) for when the dc self-bias is at its minimum and maximum. There is good agreement in trends and shape. Differences between experiment and the model may result from the assumption of there being an equal phase offset for both frequencies in the simulation. When different phases have the same dc self-bias, the mean ion energies are the same, however, the energy of the peak in the IED is different due to the different ion sheath dynamics caused by the 30 MHz. Referring to Fig. 5(a), the simulated dc biases for  $\Delta\phi_{30} = 150^\circ$  and  $30^\circ$  have similar dc bias as the  $200^\circ$  and  $20^\circ$  cases in the experiment. The corresponding IEDs are shown in Figs. 9(c) and 9(d) and have similar mean energies with different energy peak positions. These results suggest that the EAE may be used not only to control the mean ion energy region, but also to help customize the shape of the IED for different process requirements. The optimization of an etch process can be roughly divided into the rate of processing and selectivity. Selectivity depends on parameters such as the thickness of an overlying passivating polymer but selectivity more critically depends on the difference in threshold energies for ion activation between different materials.<sup>41</sup> So even with the same average ion energy, subtle changes in the IEDs (e.g., absence of a low-energy portion or enhancement of a high-energy portion) can make significant changes in the selectivity between materials.

The potential influence of EAE on plasma etching was computationally investigated using an Ar/CF<sub>4</sub>/O<sub>2</sub> = 75/20/5 gas mixture at 20 mTorr. The time-averaged plasma densities

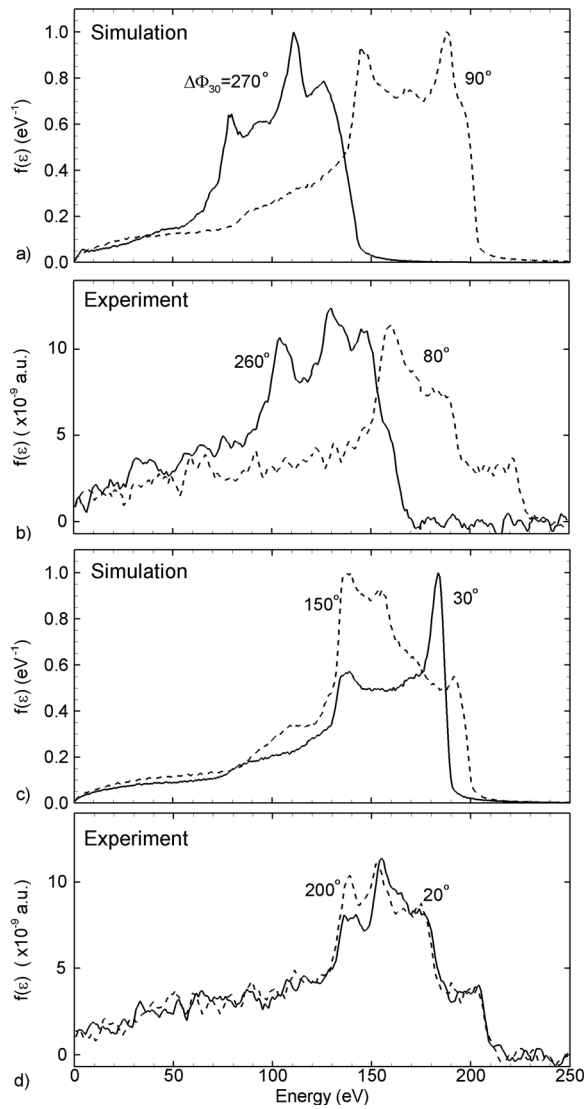


FIG. 9. Simulated and measured IEDs for operating conditions of Ar at 20 mTorr, 50 sccm,  $V_B(t) = 100V \sin(\omega_{15t} + 180^\circ) + 100V \sin(\omega_{30t} + 180^\circ + \Delta\phi_{30})$ . In the experiment, the phase delay is unknown. (a) Simulated IEDs for minimum and maximum dc-bias phases,  $\Delta\phi_{30} = 270^\circ$  and  $90^\circ$ . (b) Measured IEDs for minimum and maximum dc-bias phases,  $\Delta\phi_{30} = 260^\circ$  and  $80^\circ$ . (c) Simulated IEDs at phases that have similar dc biases,  $\Delta\phi_{30} = 150^\circ$  and  $30^\circ$ . (d) Measured IEDs for phases having similar dc biases,  $\Delta\phi_{30} = 200^\circ$  and  $20^\circ$ . The different shape of the IEDs suggests that the EAE not only affects mean ion energy but also ion sheath dynamics which modify IEDs.

were calculated to be  $1.9 \times 10^{10} \text{ cm}^{-3}$ ,  $1.5 \times 10^{10} \text{ cm}^{-3}$ ,  $1.8 \times 10^{10} \text{ cm}^{-3}$ , and  $1.8 \times 10^{10} \text{ cm}^{-3}$  for phase differences of  $\Delta\phi_{30} = 0^\circ, 90^\circ, 180^\circ$ , and  $270^\circ$ , respectively. The phase shifting has minor influence on the electronegativity and ion fluxes as well. The electronegativity varies by only 2% (between 0.17 to 0.19) over this range of  $\Delta\phi_{30}$ . The summed fluxes of major radical and ion species ( $\text{Ar}^+$ ,  $\text{CF}_3^+$ ,  $\text{O}_2^+$ ,  $\text{CF}_2$ ,  $\text{CF}_3$ ,  $\text{F}$ ,  $\text{O}$ ,  $\text{F}_2$ ) were found change to change by about 10%.

A high aspect trench was etched in  $\text{SiO}_2$  over Si with a hard mask. The phase difference  $\Delta\phi_{30}$  was varied from  $0^\circ$  to  $270^\circ$ . The resulting IEDs for  $\text{CF}_3^+$ ,  $\text{Ar}^+$ , and  $\text{O}^+$  are shown in Fig. 10. The control of IEDs by use of the EAE is complicated by the different masses of the ions. The response of

ions to the change in phase and harmonic content of the sheath is a function of their mass. Although the general trends of the IEDs for  $\text{CF}_3^+$ ,  $\text{Ar}^+$ , and  $\text{O}^+$  scale similarly with changes in  $\Delta\phi_{30}$ , the details of the individual IEDs are sensitive functions of the ion mass. The ability to control the width and location of the maximum in the IEDs scales inversely with ion mass. Small changes in the value of  $\Delta\phi_{30}$  can translate to significant changes in the etch profile as shown

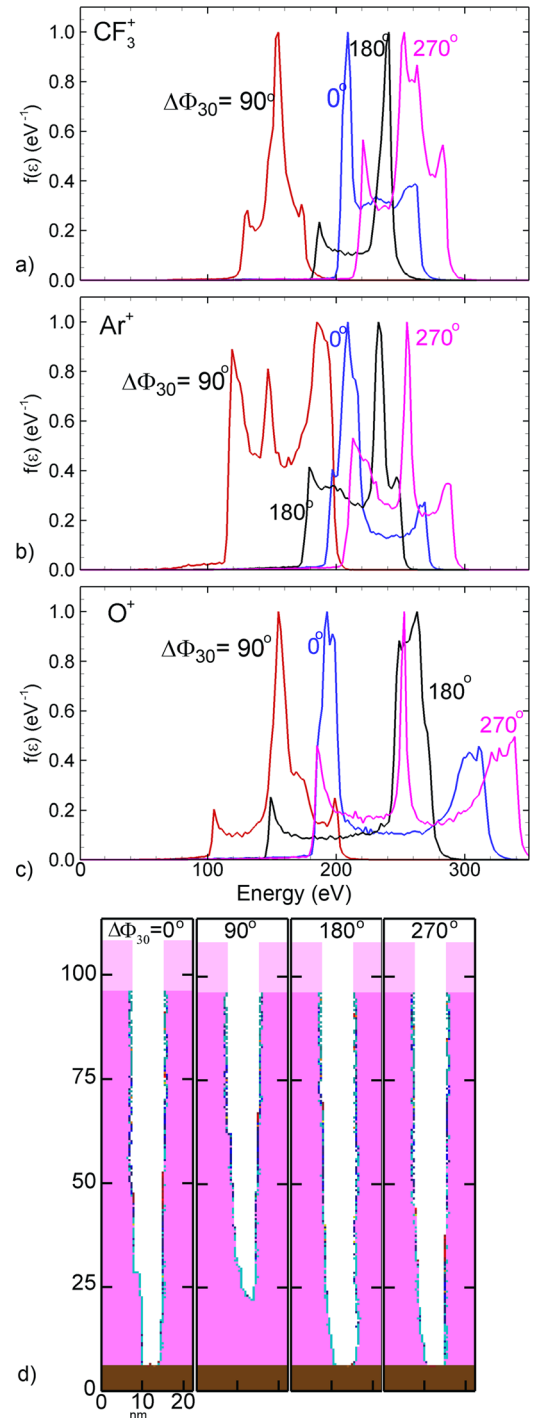


FIG. 10. Simulated IEDs and etch profiles for  $\text{Ar}/\text{CF}_4/\text{O}_2 = 75/20/5$  at 20 mTorr with  $V_B(t) = 100V \sin(\omega_{15t} + 180^\circ) + 100V \sin(\omega_{30t} + 180^\circ + \Delta\phi_{30})$ , where  $\Delta\phi_{30} = 0^\circ, 90^\circ, 180^\circ$ , and  $270^\circ$ . (a)  $\text{CF}_3^+$  (heaviest ion), (b)  $\text{Ar}^+$  (major ion species), (c)  $\text{O}^+$  (lightest ion), and (d) etch profiles when the  $\Delta\phi_{30} = 270^\circ$  case reaches 20% over-etch.

in Fig. 10(d). The profiles are plotted at the time that the profile for  $\Delta\phi_{30}=270^\circ$  reached 20% over-etch (etching continued for 20% more time than was required to reach the bottom of the feature). The etch rate of  $\text{SiO}_2$  generally scales as  $(\varepsilon_{ion}^{1/2} - \varepsilon_{th}^{1/2})$ , where  $\varepsilon_{th}$  is a threshold energy that depends on the details of the chemical system.<sup>42</sup> With this scaling, the  $\Delta\phi_{30}=90^\circ$  case has the lowest etch rate (lowest dc bias) and the  $\Delta\phi_{30}=270^\circ$  case has the highest etch rate (largest dc bias). With similar values of the mean ion energy (dc bias), the  $\Delta\phi_{30}=0^\circ$  and  $180^\circ$  cases have different etch profiles, a consequence of the shape of the IED. For example, the larger low energy peak of the IED for  $\Delta\phi_{30}=0^\circ$  case stimulates additional polymer deposition on the side walls of the feature or sputters less polymer from the side wall, which produces more tapering of the profile. The systematic trends are difficult to discern since the IEDs do not monotonically vary with phase difference  $\Delta\phi_{30}$ .

## V. PLASMA PROPERTIES AND IEDS IN A TRIPLE-FREQUENCY CCP REACTOR

Since higher ion fluxes usually translate to higher etch rates, high plasma density reactors are typically employed

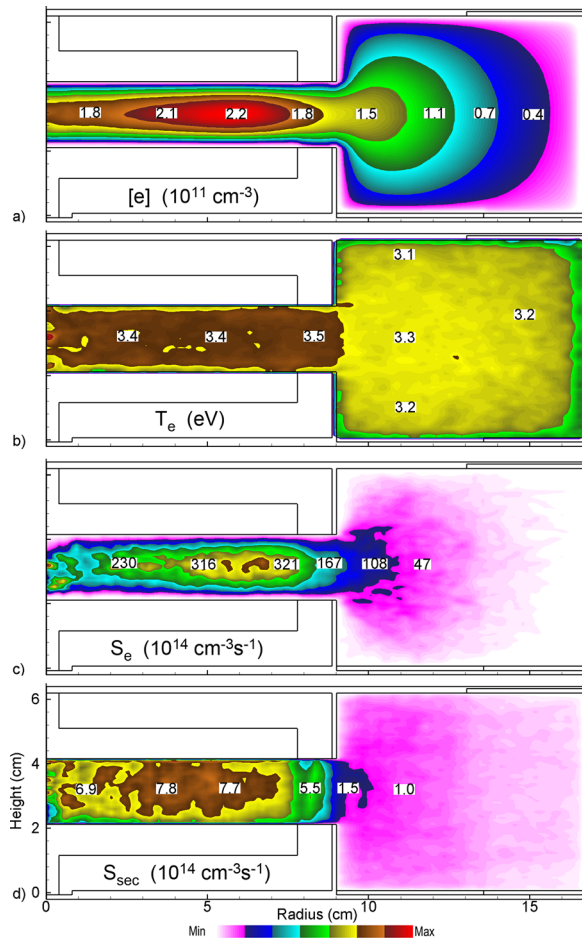


FIG. 11. Time averaged plasma properties for the TF-CCPs base case conditions (Ar, 20 mTorr, 50 sccm,  $V(t) = 100V \sin(\omega_{15}t + 180^\circ) + 100V \sin(\omega_{30}t + 180^\circ) + P_{60} \sin(\omega_{60}t + 270^\circ)$  and  $P_{60} = 150 \text{ W}$ ). (a) Electron density, (b) electron temperature, (c) bulk electron ionization source, and (d) ionization by sheath accelerated secondary electrons. The plots use linear scales.

for industrial processes. In order to attain high plasma densities in CCPs, a high frequency ( $>40 \text{ MHz}$ ) is commonly used as electron heating scales with  $\omega^2$ . To investigate the EAE with quasi-independent control of the plasma density, the top electrode was additionally powered at 60 MHz. The base case for the computations is Ar, 20 mTorr with a voltage waveform:  $V(t) = 100V \sin(\omega_{15}t + 180^\circ) + 100V \sin(\omega_{30}t + 180^\circ) + V_{60} \sin(\omega_{60}t + 270^\circ)$ . The voltage at 60 MHz was adjusted to deliver 150 W. The electron density and temperature, ionization sources by bulk electrons and by secondary electrons are shown in Fig. 11. The maximum electron density is  $2.3 \times 10^{11} \text{ cm}^{-3}$  with an average  $T_e = 3.4 \text{ eV}$ . With the addition of the 60 MHz power, the plasma density of the TF-CCP is two times larger than that of the DF-CCP. The majority of this increase comes from an increase in the bulk ionization source, a consequence of more efficient electron heating at the higher frequency. The 60 MHz power is approximately half the total. Since the 15 MHz and 30 MHz voltages are held constant, upon applying the 60 MHz power which increases the ion current, the power at 15 MHz and 30 MHz also increase.

While varying  $\Delta\phi_{30}$  in the TF-CCP while keeping all other parameters constant, the plasma uniformity at mid-gap was more sensitive to phase compared to the DF-CCF. These trends are shown in Fig. 12(a). This sensitivity was most pronounced for  $\Delta\phi_{30}=0^\circ$  for the TF-CCP (minimum in density) and  $\Delta\phi_{30}=270^\circ$  for the DF-CCP (maximum in density). When the power at 60 MHz is increased from 50

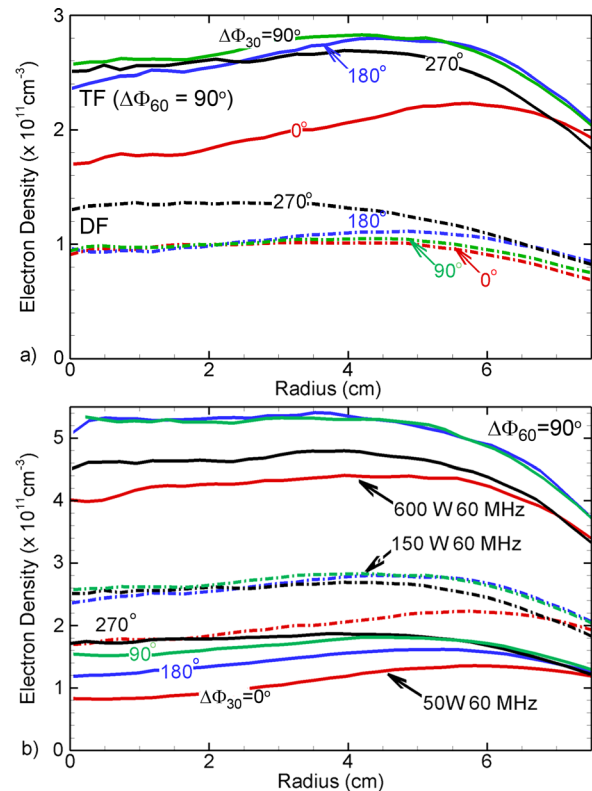


FIG. 12. Electron density at mid-gap from the center of the reactor to the edge of the electrode with bottom bias  $V_B(t) = 100V \sin(\omega_{15}t + 180^\circ) + 100V \sin(\omega_{30}t + 180^\circ) + \Delta\phi_{30}$  and  $\Delta\phi_{30}=0^\circ, 30^\circ, 60^\circ,$  and  $90^\circ$ . (a) Comparison between no 60 MHz power on top electrode (DF) and 150 W at 60 MHz (TF). (b) 60 MHz power = 50, 150, and 600 W and with constant 60 MHz phase.

600 W, the plasma density increases, though not linearly. From 50 to 600 W (a factor of 12) the plasma density increased by a factor of 3, as shown in Fig. 12(b). However, with higher power at 60 MHz, the plasma becomes more uniform, likely a consequence of the electron heating at 60 MHz being less sensitive to the electric field enhancement at the edge of the electrodes. The modulation in electron density with  $\Delta\phi_{30}$  persists for all 60 MHz powers though the value of  $\Delta\phi_{30}$  which produces the maximum density is sensitive to the 60 MHz power. At 50 W of 60 MHz power,  $\Delta\phi_{30} = 270^\circ$  produces the highest plasma density. For 600 W,  $\Delta\phi_{30} = 90^\circ - 180^\circ$  produces the highest plasma density. There are two effects that may influence these trends. First, the higher plasma density produced by 600 W at 60 MHz results in a thinner sheath which would reduce the relative value of stochastic heating at 15 and 30 MHz compared to resistive heating. Therefore, the contribution of the 30 MHz voltage to ionization may be disproportionately smaller. Second, the higher 60 MHz power requires a larger voltage at 60 MHz, which then adds more significant modulation to the sheath.

The phase setting of the 60 MHz voltage had a significant effect on plasma uniformity. The electron density at mid gap as a function of radius is shown in Fig. 13 for  $\Delta\phi_{60} = 0^\circ$  to  $270^\circ$  for  $\Delta\phi_{30} = 90^\circ$  and  $270^\circ$ . The electron density varies by 20% while changing  $\Delta\phi_{60}$  with  $\Delta\phi_{30} = 270^\circ$ . The electron density varies by 35% for  $\Delta\phi_{30} = 90^\circ$ . The  $\Delta\phi_{60}$  of the maximum density is also sensitive to  $\Delta\phi_{30}$ ,

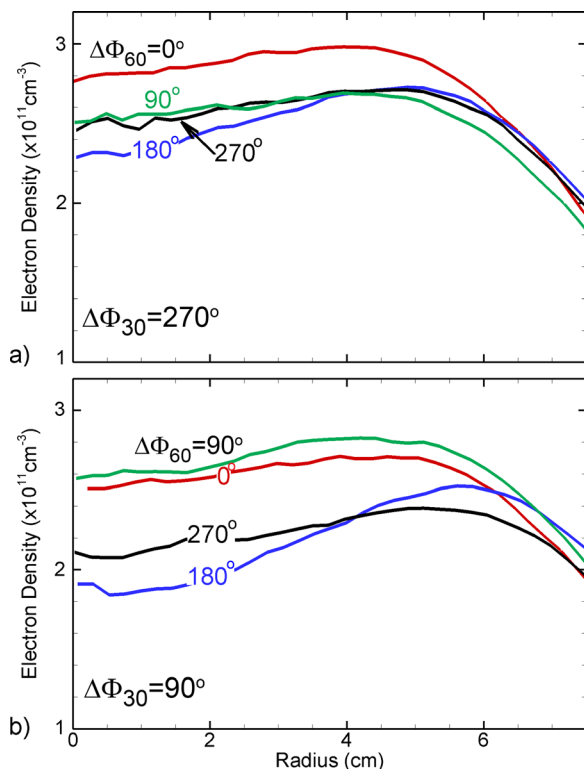


FIG. 13. Electron density at mid-gap from the center of the reactor to the edge of the electrode with bottom bias:  $V_B(t) = 100V \sin(\omega_{15}t + 180^\circ) + 100V \sin(\omega_{30}t + 180^\circ + \Delta\phi_{30})$  and 150 W on the top electrode with voltage waveform  $V_{60} \sin(\omega_{60}t + 180^\circ + \Delta\phi_{60})$  where  $\Delta\phi_{60} = 0^\circ, 90^\circ, 180^\circ,$  and  $270^\circ$ . (a)  $\Delta\phi_{30} = 270^\circ$  and (b)  $\Delta\phi_{30} = 90^\circ$ . Note that the electron density is plotted over a range of  $1.0 \times 10^{11}$  to  $3.2 \times 10^{11} \text{ cm}^{-3}$ .

and generally aligns with when the 30 MHz and 60 MHz voltages constructively interfere.

In order to verify that the EAE persists in TF-CCPs, we investigated the influence of  $\Delta\phi_{30}$  on dc bias for Ar at 10 mTorr. The 60 MHz power was constant at 150 W. The ratio of voltages at 15 MHz and 30 MHz were  $V_{15}/V_{30} = 1, 2,$  and  $3$ . The numerically and experimentally derived dc-biases are shown in Fig. 14. When adding the 60 MHz power, the EAE based on the voltages applied at 15 and 30 MHz (or 13.56 and 27.12 MHz in the experiment) still persists. However, the degree of modulation of the dc bias when changing  $\Delta\phi_{30}$  is not as great as in the absence of the 60 MHz power (see Fig. 5)—a trend borne out in both the computed and experimental results. [Note that there is an unknown phase offset of the fundamental frequency in the experiment. So the experimental results ( $V_{13} = V_{27}$  and  $V_{13} = 3V_{27}$ ) were shifted  $90^\circ$  for consistency, which then also align with the predictions as a function of phase offset.]

The predictions have a good match with the experimental measurements, as shown in Fig. 14. The modulation in the dc bias is greatest for  $V_{15} = 3V_{30}$ , and smallest for  $V_{15} = V_{30}$ . The magnitude of the dc bias increases as  $V_{15}$  increases. The modulation for  $V_{15} = V_{30}$  is symmetric through the full cycle of  $\Delta\phi_{30}$  offset and is asymmetric for  $V_{15} = 3V_{30}$ . The reduction in the depth of modulation of the dc-bias when adding the 60 MHz power is attributable to its additional contributions to the rf current. The dc bias is

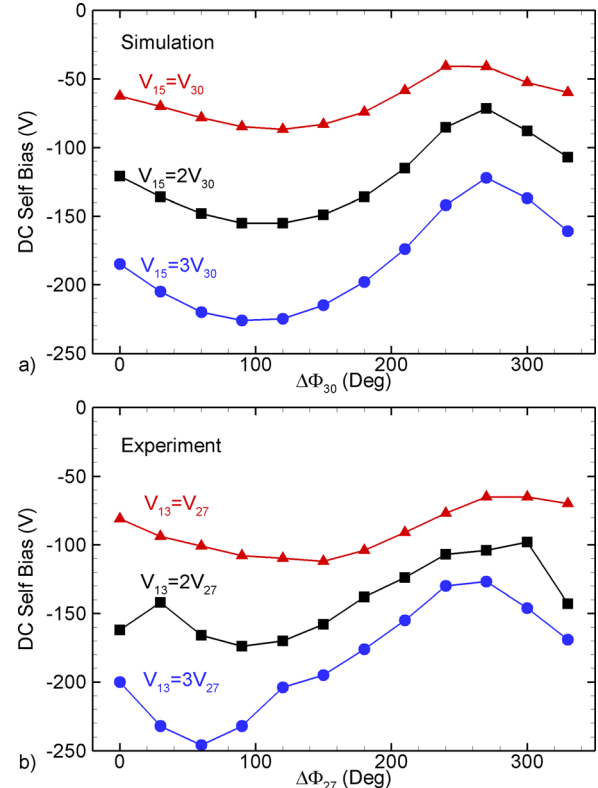


FIG. 14. EAE for TF-CCPs in Ar at 10 mTorr shown by the dc self-bias with  $\Delta\phi_{30}$  varying from  $0^\circ$  to  $330^\circ$  for voltage ratios of  $V_{30}/V_{15} = 1, 2,$  and  $3$ . Results from (a) simulation and (b) experiment.  $V_{30} = 75 \text{ V}$  in the simulation and  $V_{27}$  in experiment has an average value of 59 V with a 15% variation. Both simulation and experiment find that larger  $V_{15}$  produces a more negative dc self-bias.

ultimately determined by the relative currents collected by either side of the blocking capacitor. When adding the 60 MHz power, the fractional contribution to the current by the first and second harmonic is less. The higher plasma density provided by the 60 MHz also reduces the dependence of the sheath properties on the first and second harmonics. For example, the sheath thickness has less dependence on  $\Delta\phi_{30}$  because the plasma density is sustained by the 60 MHz power somewhat independently of the power at the first and second harmonics.

The measured and simulated IEDs for  $\Delta\phi_{30}$  varied from  $0^\circ$  to  $330^\circ$  with 150 W of power at 60 MHz in a 10 mTorr Ar plasma are shown in Figs. 15 and 16 for  $V_{15}/V_{30} = 1, 2, \text{ and } 3$ . The mean ion energy generally follows the modulation in the dc bias as  $\Delta\phi_{30}$  is varied. The ions respond most directly to the oscillation of the sheath at the lowest frequency and so the energy width of the IEDs increases in both the measured and simulated IEDs with larger  $V_{15}$ . From  $\Delta\phi_{30} = 30^\circ$  to  $180^\circ$ ,

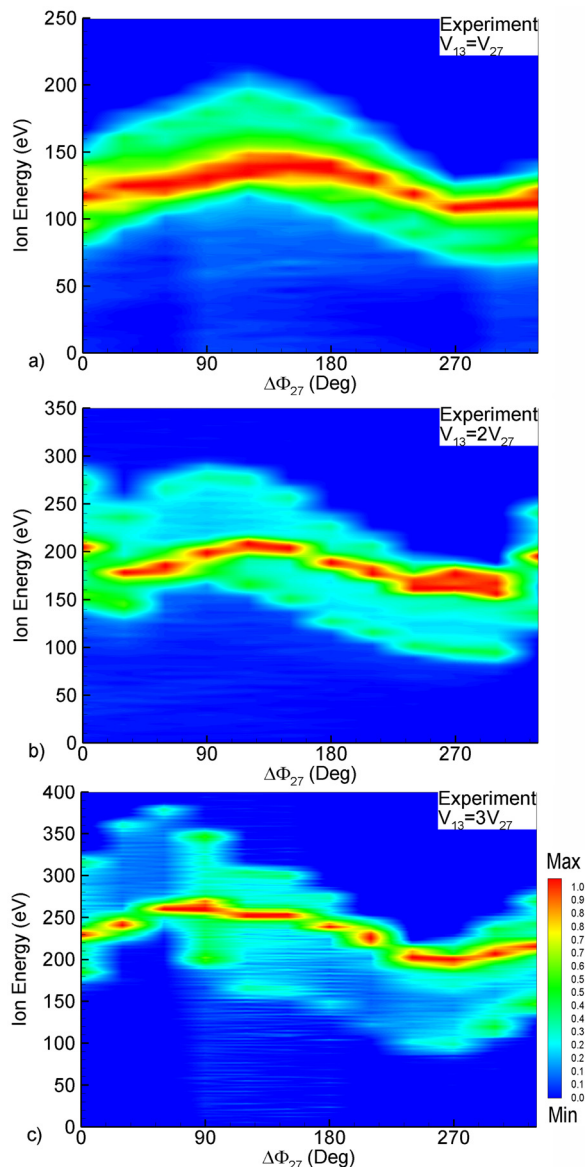


FIG. 15. Experimentally measured IEDs with 60 MHz power for  $\Delta\phi_{27}$  varied from  $0^\circ$  to  $330^\circ$  for Ar at 10 mTorr. The distributions are normalized with respect to the maximum ion energy at each phase.

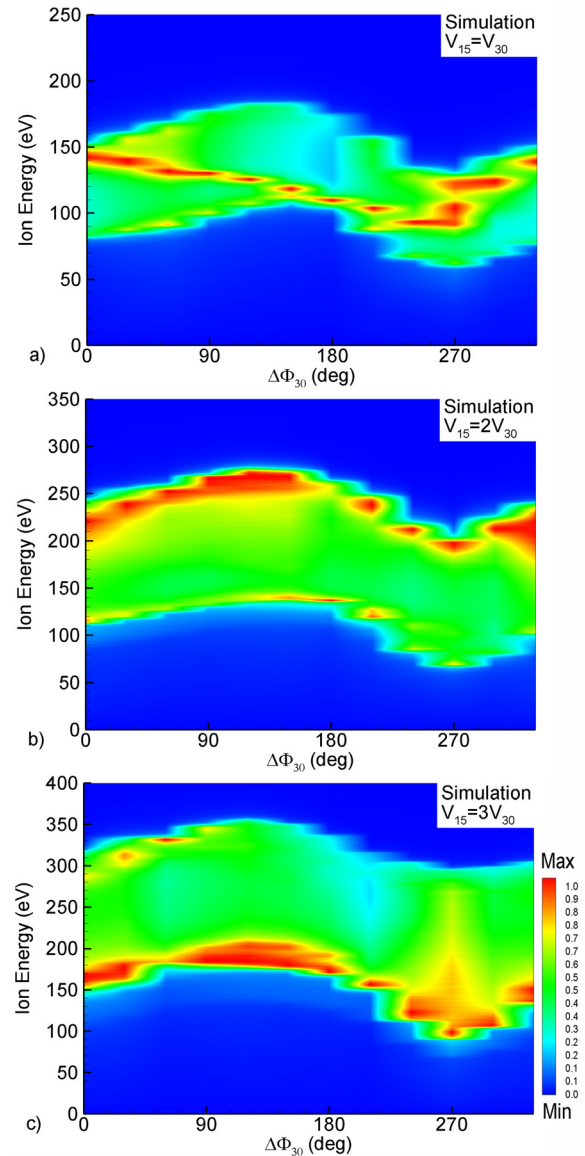


FIG. 16. Simulated IEDs with 60 MHz power for  $\Delta\phi_{30}$  varied from  $0^\circ$  to  $330^\circ$  for Ar at 10 mTorr. The distributions are normalized with respect to the maximum ion energy at each phase.

when  $V_{15} = V_{30}$  the energy width of the IED reduces from 83 eV to 62 eV in the experiment and from 83 eV to 66 eV in the simulation. A similar trend has been reported by Coumou *et al.*<sup>32</sup> for DF-CCPs. Since the voltages of the lower frequencies are kept constant, the modulation in the energy width of the IED comes from a change in the sheath thickness. The plasma density and the portion of the cycle that is cathodic varies with  $\Delta\phi_{30}$ . Higher plasma density (or a smaller fraction of the cycle that is cathodic) results in a thinner sheath, a shorter ion transit time across the sheath and a wider IED. When  $V_{15}/V_{30}$  increases, the variation in the sheath thickness is less pronounced and so the width of the IED has less variation.

The mean ion energy generally follows the dc-bias as  $\Delta\phi_{30}$  is varied. However, the energy at the peak of the IED has less variation with phase, best shown in the computed and experimental results for  $V_{15} = V_{30}$ . This means that the energy of the peak of the IED changes its position from the lower portion of the IED with small  $\Delta\phi_{30}$  to the higher

portion of the IED for large  $\Delta\phi_{30}$ . This trend is less clear for  $V_{15}/V_{30}=2$  and 3. Although the experimental IEDs show this mode of modulation for all  $V_{15}/V_{30}$ , the simulation only captures this modulation when  $V_{15}=V_{30}$ . When the voltage ratio increases, the energy of the peak of the IED stays on either the low or high energy side of the IED. The mismatch may come from the unknown phase setting of 60 MHz in the experiment.

The measured and calculated IEDs of Ar at 20 mTorr with 150 W at 60 MHz for  $\Delta\phi_{30}=270^\circ$  and  $90^\circ$  are shown in Fig. 17. Since the phase shift of the 60 MHz voltage is unknown in the experiment, we investigated the influence of  $\Delta\phi_{60}$  on the IEDs. With  $\Delta\phi_{60}$  changing from 0 to  $270^\circ$  the energy of the maximum of the IED changed by approximately half the width of the IED, while the energy widths of

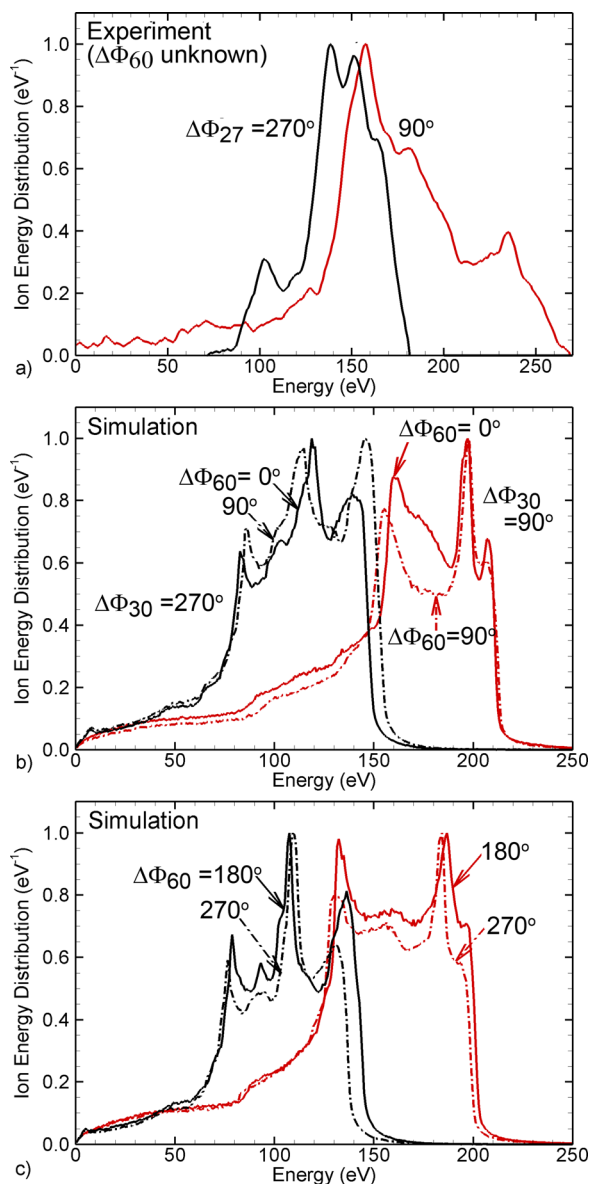


FIG. 17. IEDs with minimum and maximum dc self-bias ( $\Delta\phi_{30}=270^\circ$  and  $90^\circ$ ) for Ar at 20 mTorr with 150 W power at 60 MHz and  $V_{15}=V_{30}=100$  V. (a) Experiment with no phase lock on 60 MHz and unknown phase offset from generator to electrode. Simulated IEDs with (b)  $\Delta\phi_{60}=0^\circ$  and  $90^\circ$ , (c)  $\Delta\phi_{60}=180^\circ$  and  $270^\circ$ . In the simulation, the phase offset is estimated to be  $180^\circ$  for all frequencies.

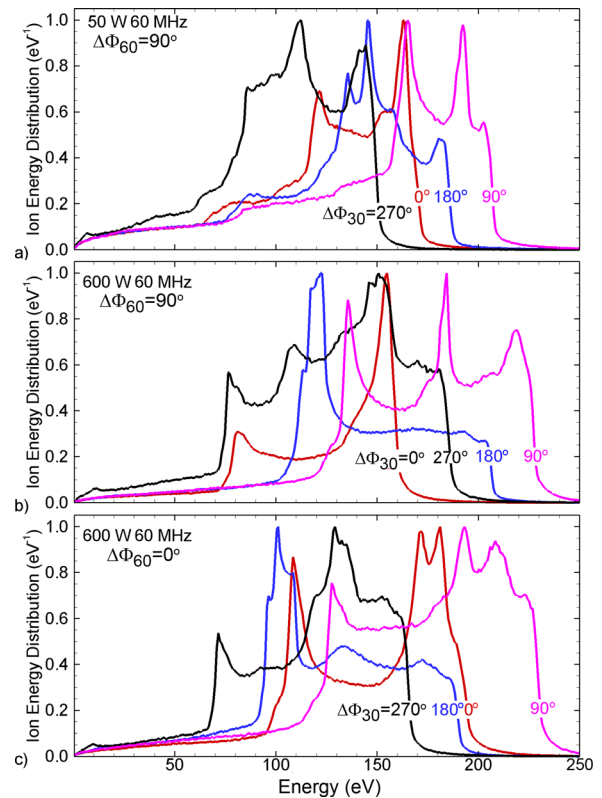


FIG. 18. IEDs for Ar at 20 mTorr with a voltage on the bottom electrode of  $V_B(t) = 100V \sin(\omega_{15}t + 180^\circ) + 100V \sin(\omega_{30}t + 180^\circ + \Delta\phi_{30})$  and power on the top electrode of  $P_{60}$  with voltage waveform  $V_{60} \sin(\omega_{60}t + 180^\circ + \Delta\phi_{60})$ . Values are shown for  $\Delta\phi_{30}=0^\circ, 90^\circ, 180^\circ,$  and  $270^\circ$ . (a)  $P_{60}=50$  W,  $\Delta\phi_{60}=90^\circ$ , (b)  $P_{60}=600$  W,  $\Delta\phi_{60}=90^\circ$ , and (c)  $P_{60}=600$  W,  $\Delta\phi_{60}=0^\circ$ .

the IEDs were modulated by about 15 eV. This modulation in the energy width of the IED most likely resulted from the variation in plasma density and so sheath thickness that occurs when varying  $\Delta\phi_{60}$ .

The influence of the 60 MHz power and value of  $\Delta\phi_{60}$  on IEDs were numerically studied as  $\Delta\phi_{30}$  was varied and the results are shown in Fig. 18. With a large 60 MHz power and a large plasma density, IEDs broadened due to the thinning of the sheath. The dc self-bias is still modulated by  $\Delta\phi_{30}$  consistent with the EAE. When the 60 MHz power is large, its voltage amplitude is large enough to modulate the sheath potential. As such, changing  $\Delta\phi_{30}$  with large 60 MHz power produces significant modulation of the positions of the peak and shapes of IEDs. (Compare the IEDs in Figs. 18(b) and 18(c)) However, for a constant 60 MHz power, the value of  $\Delta\phi_{60}$  does not significantly affect the energy widths of the IEDs.

## VI. CONCLUDING REMARKS

The consequences of the electrical asymmetry effect in DF- and TF-CCPs have been discussed with results from computational and experimental investigations. The experimental reactor was geometrically asymmetric, which naturally produced a large dc bias. The effect of the EAE on dc bias was therefore investigated in the context of a geometrically asymmetric reactor having this natural negative dc bias as one might find in industry. The general trends of the EAE

were also observed in this asymmetric system, however, the dependence of dc bias and so ion energy distributions were ultimately sensitive to the geometric asymmetry, rf voltage amplitudes and phases, and the phase offsets. The EAE has a first order effect on IEDs through not only the shift in the mean ion energy by modulation in the dc bias, but also in the shape of the IED, as represented by the energy of the peak of the IED. These trends persist in the TF-CCP where additional ionization is provided by a high frequency power source. Results from the model generally align with the experiments. Mismatches between the model and experiment may in part be explained by unknown phase offsets and phase shifts at 60 MHz.

We found that the energy of the peak of the IEDs shifts between low and high energy as  $\Delta\phi_{30}$  varies from  $0^\circ$  to  $330^\circ$ . The modulation in plasma density with changes in  $\Delta\phi_{30}$  can modulate the sheath thickness and contribute to a modulation of the energy width of IEDs at certain phases. Although the consequences on plasma density with phase shift and its correlation with harmonic currents warrants further study, the computational and experimental results discussed here show that small changes of phase translate to significant changes in plasma properties and may provide a means for customizing the shape of IEDs. These trends based on studies in argon also apply to multicomponent gas mixtures, through the trends are less clear due to the large variation in ion mass. Nevertheless, profile simulation of etching in complex gas mixtures using IEDs modulated by the EAE suggest that etch processes can be controlled through judicious choice of phase offsets between harmonic voltages.

## ACKNOWLEDGMENTS

This work was supported by Semiconductor Research Corp., Department of Energy Office of Fusion Energy Science (DE-SC0001319), the National Science Foundation (CHE-1124724 and IIP-1362103), Lam Research Corp. and MKS Instruments.

- <sup>1</sup>T. Kitajima, Y. Takeo, Z. L. Petrovic, and T. Makabe, *Appl. Phys. Lett.* **77**, 489 (2000).
- <sup>2</sup>H. C. Kim and J. K. Lee, *J. Vac. Sci. Technol. A* **23**, 651 (2005).
- <sup>3</sup>J. K. Lee, O. V. Manuilenko, N. Y. Babaeva, H. C. Kim, and J. W. Shon, *Plasma Sources Sci. Technol.* **14**, 89 (2005).
- <sup>4</sup>J. Liu, Y.-X. Liu, Z.-H. Bi, F. Gao, and Y.-N. Wang, *J. Appl. Phys.* **115**, 013301 (2014).
- <sup>5</sup>S.-B. Wang and A. E. Wendt, *J. Appl. Phys.* **88**, 643 (2000).
- <sup>6</sup>A. Agarwal, P. J. Stout, S. Banna, S. Rauf, K. Tokashiki, J.-Y. Lee, and K. Collins, *J. Appl. Phys.* **106**, 103305 (2009).
- <sup>7</sup>P. Diomede, D. J. Economou, and V. M. Donnelly, *J. Appl. Phys.* **109**, 083302 (2011).
- <sup>8</sup>E. Semmler, P. Awakowicz, and A. Keudell, *Plasma Sources Sci. Technol.* **16**, 839 (2007).

- <sup>9</sup>M. M. Turner and P. Chabert, *Plasma Sources Sci. Technol.* **16**, 364 (2007).
- <sup>10</sup>B. G. Heil, U. Czarnetzki, R. P. Brinkmann, and T. Mussenbrock, *J. Phys. D: Appl. Phys.* **41**, 165202 (2008).
- <sup>11</sup>Z. Donkó, J. Schulze, B. G. Heil, and U. Czarnetzki, *J. Phys. D: Appl. Phys.* **42**, 025205 (2009).
- <sup>12</sup>J. Schulze, E. Schüngel, and U. Czarnetzki, *J. Phys. D: Appl. Phys.* **42**, 092005 (2009).
- <sup>13</sup>Q.-Z. Zhang, W. Jiang, L.-J. Hou, and Y.-N. Wang, *J. Appl. Phys.* **109**, 013308 (2011).
- <sup>14</sup>I. Korolov, Z. Donkó, U. Czarnetzki, and J. Schulze, *J. Phys. Appl. Phys.* **45**, 465205 (2012).
- <sup>15</sup>T. Lafleur and J. P. Booth, *Appl. Phys. Lett.* **102**, 154104 (2013).
- <sup>16</sup>E. Schüngel, D. Eremin, J. Schulze, T. Mussenbrock, and U. Czarnetzki, *J. Appl. Phys.* **112**, 053302 (2012).
- <sup>17</sup>S. Bienholz, T. Styrnoll, and P. Awakowicz, *J. Phys. D: Appl. Phys.* **47**, 065201 (2014).
- <sup>18</sup>D. Hrunski, A. Janssen, T. Fritz, T. Hegemann, C. Clark, U. Schreiber, and G. Grabosch, *Thin Solid Films* **532**, 56 (2013).
- <sup>19</sup>D. Hrunski, F. Mootz, A. Zeuner, A. Janssen, H. Rost, R. Beckmann, S. Binder, E. Schüngel, S. Mohr, D. Lugenhölscher, U. Czarnetzki, and G. Grabosch, *Vacuum* **87**, 114 (2013).
- <sup>20</sup>B. Bruneau, T. Novikova, T. Lafleur, J. P. Booth, and E. V. Johnson, *Plasma Sources Sci. Technol.* **23**, 065010 (2014).
- <sup>21</sup>B. Bruneau, T. Novikova, T. Lafleur, J. P. Booth, and E. V. Johnson, *Plasma Sources Sci. Technol.* **24**, 015021 (2015).
- <sup>22</sup>J. Schulze, E. Schüngel, Z. Donkó, and U. Czarnetzki, *Plasma Sources Sci. Technol.* **20**, 015017 (2011).
- <sup>23</sup>T. Lafleur, P. A. Delattre, E. V. Johnson, and J. P. Booth, *Appl. Phys. Lett.* **101**, 124104 (2012).
- <sup>24</sup>A. Derzsi, I. Korolov, E. Schüngel, Z. Donkó, and J. Schulze, *Plasma Sources Sci. Technol.* **22**, 065009 (2013).
- <sup>25</sup>P. A. Delattre, T. Lafleur, E. V. Johnson, and J. P. Booth, *J. Phys. D: Appl. Phys.* **46**, 235201 (2013).
- <sup>26</sup>M. J. Kushner, *J. Phys. D* **42**, 194013 (2009).
- <sup>27</sup>S.-H. Song and M. J. Kushner, *Plasma Sources Sci. Technol.* **21**, 055028 (2012).
- <sup>28</sup>P. Tian and M. J. Kushner, *Plasma Sources Sci. Technol.* **24**, 034017 (2015).
- <sup>29</sup>A. V. Vasenkov, X. Li, G. S. Oehrlein, and M. J. Kushner, *J. Vac. Sci. Technol. A* **22**, 511 (2004).
- <sup>30</sup>R. J. Hoekstra, M. J. Grapperhaus, and M. J. Kushner, *J. Vac. Sci. Technol. A* **15**, 1913 (1997).
- <sup>31</sup>A. Sankaran and M. J. Kushner, *J. Vac. Sci. Technol. A* **22**, 1260 (2004).
- <sup>32</sup>D. J. Coumou, D. H. Clark, T. Kummerer, M. Hopkins, D. Sullivan, and S. Shannon, *IEEE Trans. Plasma Sci.* **42**, 1880 (2014).
- <sup>33</sup>D. J. Coumou and M. Kirk, U.S. patent 6707255 (March 16, 2004).
- <sup>34</sup>G. F. Franklin, J. D. Powell, and D. Workman, *Digital Control of Dynamic Systems* (Addison Wesley, Reading, MA, 1998).
- <sup>35</sup>A. Grebennikov, *RF and Microwave Transistor Oscillator Design* (Wiley, West Sussex, England, 2007).
- <sup>36</sup>D. J. Coumou, U.S. patent 6522121 (Feb. 18, 2003).
- <sup>37</sup>D. Gahan, B. Dolinaj, and M. B. Hopkins, *Rev. Sci. Instrum.* **79**, 033502 (2008).
- <sup>38</sup>A. V. Phelps, *J. Phys. Chem. Ref. Data* **20**, 557 (1991).
- <sup>39</sup>J. Schulze, E. Schüngel, U. Czarnetzki, and Z. Donkó, *J. Appl. Phys.* **106**, 063307 (2009).
- <sup>40</sup>J. Schulze, E. Schüngel, U. Czarnetzki, M. Gebhardt, R. P. Brinkmann, and T. Mussenbrock, *Appl. Phys. Lett.* **98**, 031501 (2011).
- <sup>41</sup>S.-B. Wang and A. E. Wendt, *J. Vac. Sci. Technol. A* **19**, 2425 (2001).
- <sup>42</sup>D. C. Gray, I. Tepermeister, and H. H. Sawin, *J. Vac. Sci. Technol. B* **11**, 1243 (1993).